Nuclear Science and Techniques (2026) 37:82
https://doi.org/10.1007/s41365-026-01890-w

Software and layout optimization of HIRFL-CSR external-target experiment

Jian-Wang Hong[1,2] · Chen-Lu Hu[1,2] · Yu-Hong Yu[1,2,3] · Nu Xu[1,2,3] · Zhi-Yu Sun[1,2,3] · Hao Qiu[1,2,3] · Zhi-Gang Xiao[4] · Ming Shao[5] · Li-Min Duan[1,2,3] · Xiong-Hong He[1,2,3] · Zhi-Hui Xu[1] · Yi Wang[6] · Dong Han[6] · Zi-Xuan Chen[1,2] · Feng-Yi Zhao[1,2,3] · He-Run Yang[1,2] · Xiang-Lun Wei[1,2] · Rong-Jiang Hu[1,2] · Feng Liu[7] · Hua Pei[7] · Ya-Ping Wang[7] · Ye Tian[1,2] · Zhi Qin[4] · Dong-Dong Hu[5] · Guo-Dong Shen[1,2] · Li-Jun Mao[1,2] · Wei Wu[1,2] · Wei You[1,2] · Yu-Quan Chen[1,2] · Peng Yang[1,2] · De-Qing Fang[8,9] · Ya-Peng Zhang[1,2,3]

Received: 13 February 2025 / Revised: 24 June 2025 / Accepted: 26 June 2025 / Published online: 11 February 2026

Abstract
Heavy-ion collisions (HICs) is a unique experimental tool for investigating the properties of nuclear matter under extreme conditions in the laboratory. At HIRFL-CSR energies, HICs can create nuclear matter with 2–3 times the saturation density (ρ_0). The HIRFL-CSR external-target experiment (CEE) is a large-acceptance spectrometer designed to explore frontier topics in high-energy nuclear physics, such as the QCD phase structure and nuclear matter equation of states. In this letter, we introduce simulation and analysis software for the CEE experiment (CeeROOT). Based on the CEE conceptual design and CeeROOT software, the configurations of its subdetectors were optimized by considering foreseeable physical constraints. The final detector layout of the CEE spectrometer and its acceptances were validated through simulations of U+U collisions at 500 MeV/u and pp collisions at 2.8 GeV, which demonstrated that the CEE experiment will serve as a detector with wide acceptance and multi-particle identification capabilities for studying high-energy nuclear physics topics at HIRFL-CSR energies with pp, pA, and AA collisions.

Keywords CEE experiment · Simulation software · Optimization · HIRFL-CSR

1 Introduction

Heavy-ion collisions (HIC) is a unique tool for creating hot and dense nuclear matter in the laboratory [1], which allows one to study the bulk properties of nuclear matter under extreme conditions, such as the quantum chromodynamics (QCD) phase structure [2–6] and equation of state (EoS) [7–9]. Heavy-Ion Research Facility at Lanzhou-cooling storage ring (HIRFL-CSR) can provide heavy-ion beams with kinetic energy up to 1.1 GeV/u, such as ^{12}C beam, the maximum kinetic energy of $^{238}U^{74+}$ beam is 500 MeV/u, and the maximum kinetic energy of the proton beam is 2.8 GeV [10]. HICs at HIRFL-CSR energies, nuclear matter with 2–3 ρ_0 and a temperature of ~40 MeV can be created [11, 12], which is also called as "fireball". The CSR external-target experiment (CEE) is a large-acceptance spectrometer [13] that aims to explore the properties of nuclear matter using heavy-ion and proton beams provided by the HIRFL-CSR accelerator [14].

Net-baryon higher-order cumulants are predicted to be sensitive observables for probing QCD critical points [15, 16]. The CEE experiment will precisely measure the high-order proton cumulant at 500 MeV/u U+U collisions corresponding $\sqrt{s_{NN}}$ =2.14 GeV, which will provide a strong constraint for the fluctuation behavior of the pure hadronic phase. As indicated by recent STAR flow measurements, nuclear matter created in HICs at $\sqrt{s_{NN}}$ <3 GeV is dominated by hadronic matter [17]. Currently, proton high-order cumulants at the lowest collision energy were provided by the HADES experiment at $\sqrt{s_{NN}}$ =2.4 GeV in Au+Au

This work was supported by the Strategic Priority Research Program of Chinese Academy of Sciences (No. XDB34030000), the National Natural Science Foundation of China (Nos. 11927901 and 12475133), the Youth Team Program in Basic Research Fields Stably Supported by the Chinese Academy of Sciences (No. YSBR-088), and the Western Light Project of the Chinese Academy of Sciences.

Extended author information available on the last page of the article

collisions with relatively large uncertainties [18]. Properties of the EoS in the high-density region of $\rho > 2\rho_0$, especially the part called symmetry energy E_{sym} related to isospin asymmetry $\delta = (\rho_{\mathrm{n}} - \rho_{\mathrm{p}})/(\rho_{\mathrm{n}} + \rho_{\mathrm{p}})$ (ρ_{p} proton density, ρ_{n} neutron density), are crucial for understanding QCD theory and other important phenomena such as the inner structure of neutron stars, neutron star mergers, and HIC dynamics [19–21]. Because ^{238}U is a natural nucleus with the largest isospin asymmetry, the fireball created in ^{238}U+^{238}U collisions at HIRFL-CSR energies is predicted to be an ideal environment for investigating the behavior of E_{sym} in the density $\rho > 2\rho_0$ region [20]. Other topics in the high-baryon density region, such as the subthreshold production of strangeness [22], cluster formation mechanism [23], short-range correlation [24] and hypernuclear physics [25], can also be investigated using CEE experiments.

The CEE conceptual design was described in Ref. [13], including a superconducting dipole magnet, a time projection chamber (TPC) [26], an inner time of flight detector (iTOF) [27], a multi-wire drift chamber array (MWDC) [28–30], an external time of flight detector (eTOF) [31], a zero degree calorimeter (ZDC) [32] and a beam monitoring detector [33]. The TPC and MWDC are tracking detectors covering the backward and forward regions, respectively, which are designed to measure the trajectories and energy loss ($\mathrm{d}E/\mathrm{d}x$) of charged particles. By correlating the reconstructed momentum and $\mathrm{d}E/\mathrm{d}x$, light-charged particles such as $\pi^{\pm}$, p, d, t, ^{3}He, and ^{4}He can be identified. The iTOF covers the left, right, and bottom sides of the TPC. The eTOF accepts charged particles that pass through the MWDC. By combining the momentum measured by the TPC (MWDC) and the time of flight measured by the iTOF (eTOF), charged particles can be further identified, especially for those with high-momenta. ZDC is designed for determining the reaction plane of heavy-ion collision event by event [34].

In transitioning from the conceptual design to the technical design of the CEE spectrometer, foreseeable physical constraints in the actual experiment must be addressed to ensure the fair performance of the CEE detection system. For instance, the background and side effects of the primary beam on the CEE subdetectors require careful consideration. Reactions between the beam and detector frames should be avoided. The acceptance of the subdetectors should be optimized to its theoretical limit without increasing the budget. These constraints must be considered in the final design of the CEE spectrometer.

This remainder of this letter is organized as follows. Section 2 introduced a simulation and analysis software package for the CEE experiment, called CeeROOT. In Sect. 3, the CEE layout optimization for each subdetector and their acceptances after optimization are described. In Sect. 4, the acceptance for the reaction pp→p$K^+\Lambda$ at 2.8 GeV is discussed. The final part is a summary of the current construction status and future physics program of the CEE experiment.

2 Simulation and analysis software of the CEE experiment

Simulation software is an essential part of modern particle and nuclear physics experiments for detector configuration optimization, physics feasibility studies, efficiency evaluation, and so on. The CeeROOT package is established based on the FairSoft package and FairROOT platform [35]. FairSoft is a collection of open-source software, and its compatibility has been tested across various operating systems. FairROOT is a general simulation and analysis framework for nuclear and particle physics experiments that defines general rules for detector geometry, particle definition, interfaces for various particle propagation engines, input/output (I/O) rules, event display interface, run-time database, and so on. With the same detector configuration, detector responses can be simulated using Geant3 [36] or Geant4 [37], which are widely used Monte Carlo (MC) packages for simulating interactions between particles and materials.

CeeROOT is a FairROOT realization for the CEE experiment. In general, CeeROOT includes the detector geometry of all CEE subdetectors, event generator, magnetic field, digitization, calibration software, tracking software, and event reconstruction software. In the simulation, the interactions of particles generated by various event generators (see Sect. 2.1) and detectors were simulated using the GEANT package. The information left by particles inside the sensitive volume of the detectors is further digitized according to their specific detection mechanisms. After digitization, the MC data are stored in a predefined format, which is also used for the experimental data. This enables the software to handle both MC and experimental data in the subsequent steps of calibration, reconstruction, and analysis. A flowchart of the CEE simulation and data analysis is shown in Fig. 1. In the CeeROOT package, a fast simulation was also developed to evaluate the detector performance and physics feasibility study by parameterizing the performances of all subdetectors. In the following subsections, the basic components of the CeeROOT package are briefly introduced.

2.1 Event generator

The event generator is a basic component for defining the input particle species and their initial coordinate and momentum distributions (Fig. 1). Besides simple event generators like box generator (flat phase space distribution), the simulation data of several transport models like UrQMD [38], GiBUU [39], PHSD [40], AMD [41], IQMD [42], JAM [43], LQMD [44] and PLUTO [45] are supported as well.

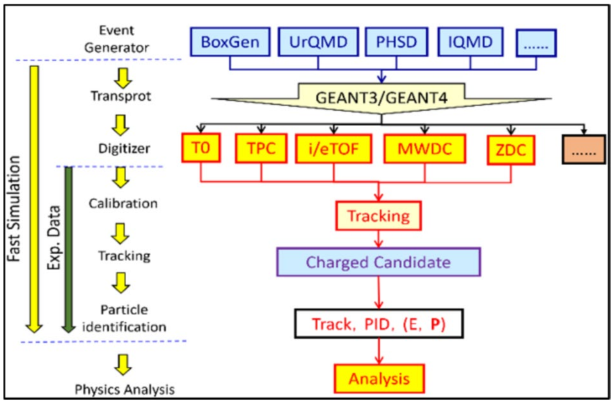

Fig. 1 (Color online) Flow chart of the CEE simulation and data analysis procedure

Table 1 Event generators of CeeROOT

Generator	Description
Box	Flat distribution of phase space
Urqmd	f14 format output of Urqmd model
GiBUU	Les-Houches Format output of GiBUU model
PHSD	PHSD model output
XiaoGen	Phase space distribution based on FOPI data
Pluto	Pluto ROOT format output
AMD	AMD model output
Pythia 6/8	Pythia 6/8 output
IQMD	IQMD model output
JAM	JAM model output
LQMD	LQMD model output

Table 1 shows the event generators currently supported by CeeROOT. In addition to the particles listed in the particle data book [46], ions with different charge states can also be defined, which allows one to simulate the trajectories and responses of ions with different charge states in the CEE spectrometer.

2.2 Magnetic field

The CEE spectrometer has superconducting dipole magnet for deflecting charged particles. The momenta of charged particles can be reconstructed by measuring their trajectories in a magnetic field. The height, width, and length of the available space inside the magnet were 1.6, 3.2, and 3.4 m, respectively. The coordinate origin of the CEE spectrometer was defined at the center of the magnet. The center of the TPC was placed at the center of the magnet. The designed strength of the magnetic field was 0.5 T with a uniformity of less than ± 2.5% in the sensitive volume of the TPC. Because it is a dipole magnet, the magnetic field varies toward both entrances. The magnetic field of the CEE magnet is described by grid data including six variables, that is, (x, y, z, B_x, B_y, B_z), where (x, y, z) are the space coordinates and (B_x, B_y, B_z) are the corresponding magnetic field vectors. The positive direction of the Z-axis represents the beam direction, while the X and Y axis complete a right-handed Cartesian coordinate system. B_y field map at the $y = 0$ cm plane is shown in Fig. 2a. Figure 2b shows absolute value of B_y along the Z-axis, the shielding region indicate a magnetic field shield pipe and a dip around $z = -320$ cm is a regulation dipole magnet. The reasons why we need these two additional components will be discussed in Sect. 3.2. In the GEANT simulation, charged particles are propagated in fine steps, where magnetic field data are required to propagate the particle to the next spatial point. The magnetic field vector at any spatial point is obtained by linear extrapolation using grid data.

In the simulation, the magnetic field data were provided by the magnet design software. The magnetic field of the CEE magnet will be measured when the magnetic field reaches its working condition, and the measured grid data will be used for the simulation and track reconstruction of the experimental data.

3 Layout optimization of the CEE spectrometer

In CEE detector layout optimization, the detector components and detector types adopted in the conceptual design are retained. The physical constraints for each subdetector are discussed. To avoid foreseeable drawbacks, the optimized detector configuration and optimization results are discussed in the following subsections.

3.1 TPC layout optimization

The TPC of the CEE spectrometer is designed to measure the energy loss and trajectories of light charge particles such as $\pi^{\pm}$, $K^{\pm}$, p, d, t, ^{3}He and ^{4}He. In the conceptual design, a heavy-ion beam, such as ^{238}U, was allowed to pass through the TPC drift volume. Tremendous ionization is expected to be induced by the heavy-ion beam in the drift volume of the TPC. This causes two major issues: 1) the TPC electronics are continuously saturated along the beam path, and 2) the ionization left by the beam causes a large space charge accumulation, which may distort the drifting electric field of the TPC. These effects not only cause difficulties in measuring the tracking of charged particles in the region along the beam path, but may also potentially damage the TPC readout electronics. To avoid these effects, the TPC is divided into two parts,

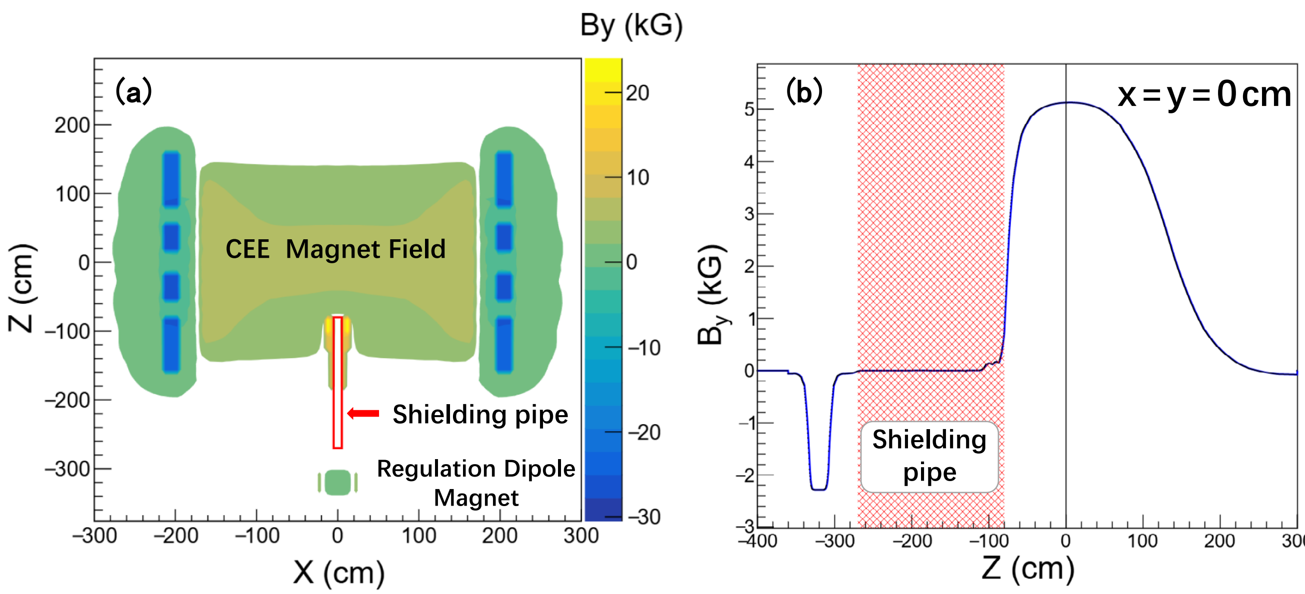

Fig. 2 (Color online) **a** Field map of B_y at the Y=0 plane of designed CEE magnet, shielding pipe and regulation dipole magnet are indicated; **b** B_y projection along the Z-axis

with a vertical gap left in between to exclude the space region where the beam passes through. The width of the gap is related to the deflection distance of the beam in the x-direction, which depends on the ion type, energy, and charge state of the beam particle. The narrower the air gap, the greater is the acceptance of the TPC.

To reduce the deflection effect of the beam, a magnetic shielding pipe and small regulation magnet were added in front of the TPC, as shown in Fig. 2. Eventually, it is proven that a gap with a width of $\pm$7.5 cm is sufficient for all types of beams provided by the HIRFL-CSR. The active volumes of the two TPCs are in the range of 10 cm < $|x|$ <60 cm, height of $-$40 cm < y <40 cm, and a length in the z direction of –45 cm < y <45 cm. Based on this TPC geometry configuration, the TPC acceptances at different emission positions along the beam axis were evaluated using U+U collisions generated by the JAM model. The TPC acceptance for $\pi^{\pm}$ reached its maximum when the initial emission position was at (0, 0, –35) cm. Consequently, this position was designated as the target position for the CEE experiment. Figure 3 shows transverse momentum (p_{T}) and rapidity (y) acceptance of the TPC for proton (left panel) and π^{+} (right panel) in U+U at 500 MeV/u simulated by the JAM model in most central collisions. The criterion for accepting a charged particle in the TPC is that its track length in the TPC active volume should exceed 15 cm. The TPC covered a polar angle range of 5° to 120° in the laboratory frame. However, the TPC has an acceptance deficiency in the azimuthal ϕ direction around 90° and 270° owing to the existence of a vertical gap. For future CEE experiments, this coverage loss must be corrected according to the TPC acceptance for each particle species.

3.2 Beam path simulation and magnetic shield pipe

To avoid beam hits on the detector frame, the beam path is a major geometrical reference for optimizing the air gap of the TPC and placing downstream detectors such as the third MWDC, eTOF, and ZDC. The typical beams used in the CEE experiment are $^{12}C^{6+}$ at 400 and 1000 MeV/u, and $^{238}U^{74+}$ at 500 MeV/u. Before the heavy-ion beam reaches the target, it passes through a Ti foil with a thickness of 30 µm for sealing the vacuum pipe, and then propagates in the air for more than 1 m. The charge state of a light ion beam, such as $^{12}C^{6+}$ beam, would not change, but the heavy-ion beam $^{238}U^{74+}$ would turn to Uranium ions with charge states of approximately 90, that is, $^{238}U^{90+}$ according to a calculation using the ETACHA4 code [47]. Thus, $^{238}U^{90+}$ ion was used for the beam path simulation instead of the beam ion $^{238}U^{74+}$.

As discussed in the previous subsection, minimizing the deflection effect for beams is crucial for narrowing the gap width of the TPC, thereby increasing its geometric acceptance. To achieve this goal, a small dipole

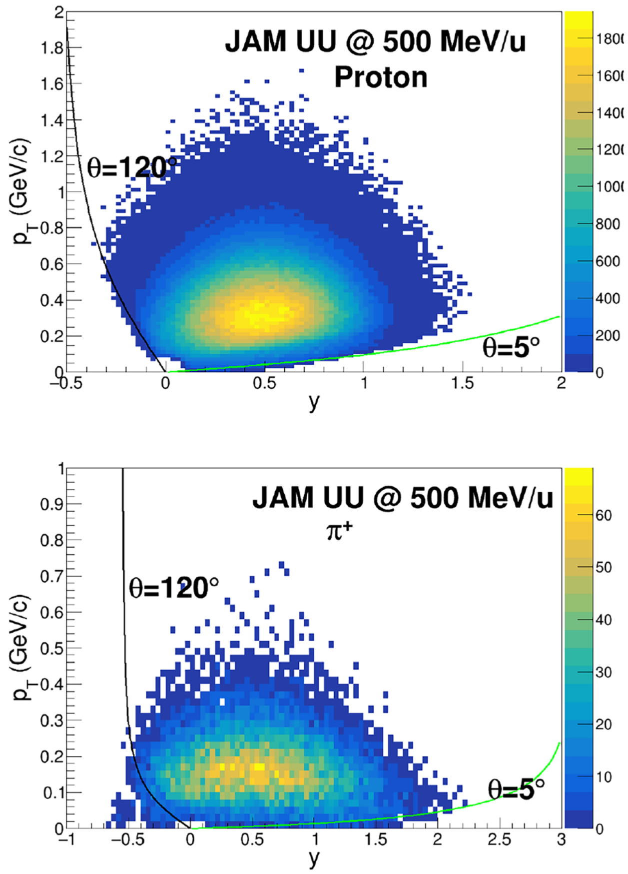

Fig. 3 (Color online) TPC acceptance for proton (left) and π (right) in U+U collisions at 500 MeV/u simulated by the JAM model, expressed in terms of transverse momentum (p_T) and rapidity (y)

magnet and magnetic shield pipe were added upstream. The polarity of the small dipole magnet is opposite to that of the CEE magnet, as shown in Fig. 2. This configuration induced a position offset for the beam, which partially counteracted the deflection effect caused by the CEE magnet. The shielding pipe spans from –290 cm to –80 cm, as shown in Fig. 2. The paths of beam $^{12}C^{6+}$ at 400 and 1000 MeV/u, $^{238}U^{90+}$ at 500 MeV/u are simulated, including the regulation magnet, shield pipe, and CEE magnet. To consider the energy loss of the beam in air, the medium in the simulation was set to air. The initial spatial and momentum distributions at a plane of $z = -400$ cm were set to be a Gaussian distribution with position divergence $\sigma_x = \sigma_y = 0.15$ cm and relative momentum divergence $\Delta P_{x/y}/P = 0.1\%$, respectively, which are the typical spatial and momentum spreads of heavy beams at the CEE experimental hall.

Figure 4a–c shows simulated beam paths of $^{12}C^{6+}$ at 400 and 1000 MeV/u, and $^{238}U^{90+}$ at 500 MeV/u in the x-z plane, respectively. In each panel, the solid line with vertical bars presents the center of the simulated beam, the vertical bars represent σ of the beam spatial spread in the X-axis, and the dashed lines mark the 5σ position spread of the beam along the X-axis. The TPC detector frame and target are also depicted in the figure. Under the current design, all these considered beams can pass through the gap without hitting the TPC detector frame. To adopt different beams, downstream subdetectors, such as eTOF and ZDC, are installed on a rail parallel to the X-axis.

3.3 MWDC and eTOF layout optimization

In the conceptual design, the MWDC and eTOF are placed outside the magnet, and their two-arm detector configuration geometrically prevents charged particles emitted in the forward region from being fully covered by the MWDC-eTOF subdetectors. To increase the forward angle acceptance, two MWDCs are placed inside the magnet after the TPC, and the third MWDC is placed outside the magnet, which almost completely covers the downstream entrance of the magnet. The eTOF was placed after the third MWDC. The active area of the eTOF is designed to contain all charged particles that pass through all three MWDCs. To avoid the beam hitting the detector frame of the MWDC and eTOF, the MWDCs and eTOF have an inactive region in the middle. Figure 5 shows acceptance of MWDC and eTOF in polar angle (θ) and azimuthal angle (ϕ) for proton in U+U collisions at 500 MeV/u simulated by the JAM model. MWDC-eTOF

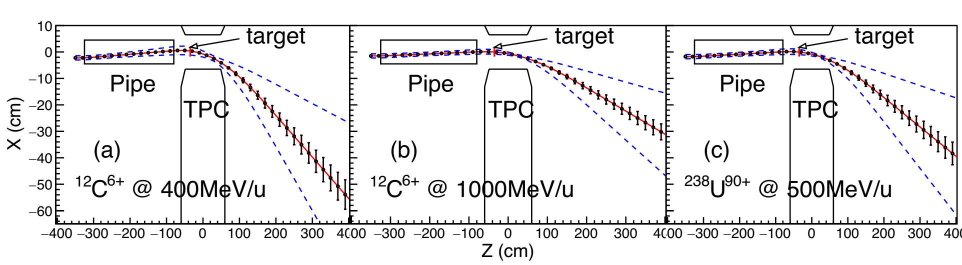

Fig. 4 (Color online) Simulated beam paths of $^{12}C^{6+}$ at 400 MeV/u (**a**), $^{12}C^{6+}$ at 1000 MeV/u (**b**) and $^{238}U^{90+}$ at 500 MeV/u (**c**) in the x-z plane, solid line indicates the central position of beam, vertical bar represents σ of spacial spread in X-axis, and dashed lines mark 5 σ spacial spread in the X-axis

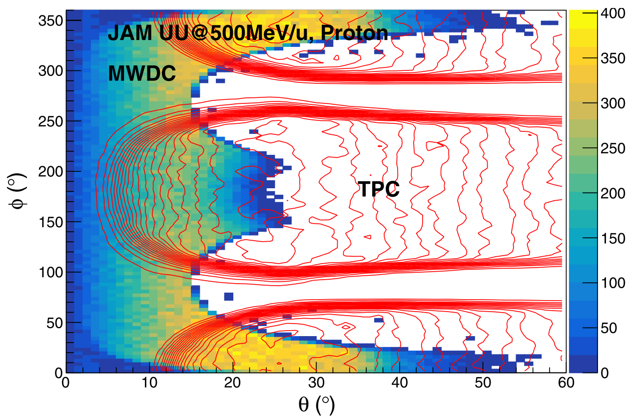

Fig. 5 (Color online) Acceptance of MWDC-eTOF (color) and TPC (contour line) in $\theta - \phi$ plane for protons in U+U collisions at 500 MeV/u simulated by the JAM model

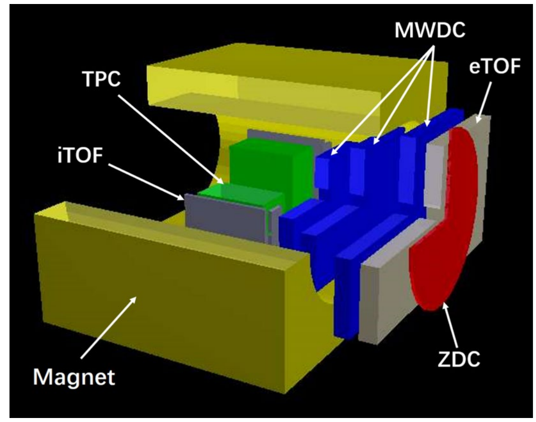

Fig. 6 (Color online) The CEE detector configuration after the optimization

covers a polar angle range of $5° < \theta < 15°$ and azimuthal angle of $0° < \phi < 360°$. Owing to the rectangular shape of the MWDCs and eTOF detectors, particles emitted at large polar angles can also be contained. The TPC acceptance for protons in the same collision system is shown in Fig. 5, depicted by contour lines. One can see that there are overlapping acceptance regions for TPC and MWDC, which can be used for calibrating tracking detectors each other.

3.4 ZDC detector optimization

ZDC is mainly designed to measure the event plane of HICs, and its hit multiplicity also helps to determine the collision centrality [34, 48]. In the conceptual design, the ZDC is designed as a calorimetric type of detector, placed downstream to measure the energy and position of heavy fragments emitted at a small polar angle. Considering that the energy resolution of the hadronic calorimeter at the HIRFL-CSR energy range is difficult to achieve high precision, the ZDC was redesigned to measure the energy loss and hit position of particles emitted in the forward region. This type of design has been successfully used in other experiments, such as the FOPI experiment [49] and the STAR experiment [50].

In the new design, the ZDC is a plastic scintillator disk with inner and outer radii of 5 and 100 cm, respectively. ZDC is divided into 8 rings, each ring contains 24 sectors. It has 192 plastic scintillator modules. The ZDC is placed immediately after the eTOF. As mentioned above, to adopt different beams, the ZDC is installed on a horizontal rail, and its position along the X-axis can be adjusted. An event plane reconstruction algorithm based on the ZDC was developed, which showed an excellent reaction plane resolution based on the simulated data [34].

3.5 Final detector configuration and technical design

Finally, the optimized detector configuration of the CEE experiment was accomplished, as shown in Fig. 6. Based on the optimized configuration, the technical design of the CEE spectrometer was achieved by considering realistic detector frames and their geometry compatibilities, as shown in Fig. 7. As mentioned above, (0, 0, −35) cm is the nominal target position of CEE experiment, which is just located in the TPC air gap. The designed reaction rate of the CEE experiment reaches up to 10 kHz for heavy-ion collisions, such as U+U collisions. The typical momentum resolution and TOF time resolution of the CEE experiment are 5% and < 80 ps, respectively, according to a fast simulation [14], and charged particles, i.e $\pi^{\pm}$, p, d, t, ^{3}He, and ^{4}He, can be well identified. By combining the TPC and MWDC, the CEE spectrometer can cover >80% of the protons produced in 500 MeV/u U+U collisions simulated by the JAM model. These features make the CEE an

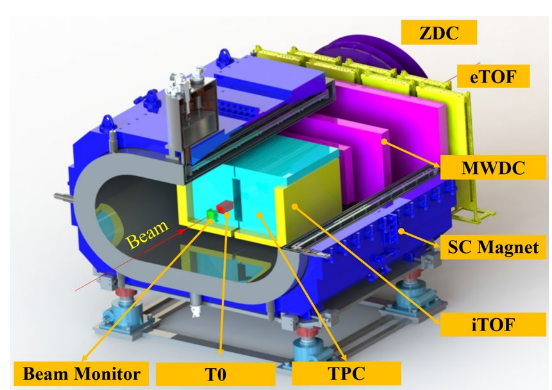

Fig. 7 (Color online) Technical design of the CEE spectrometer

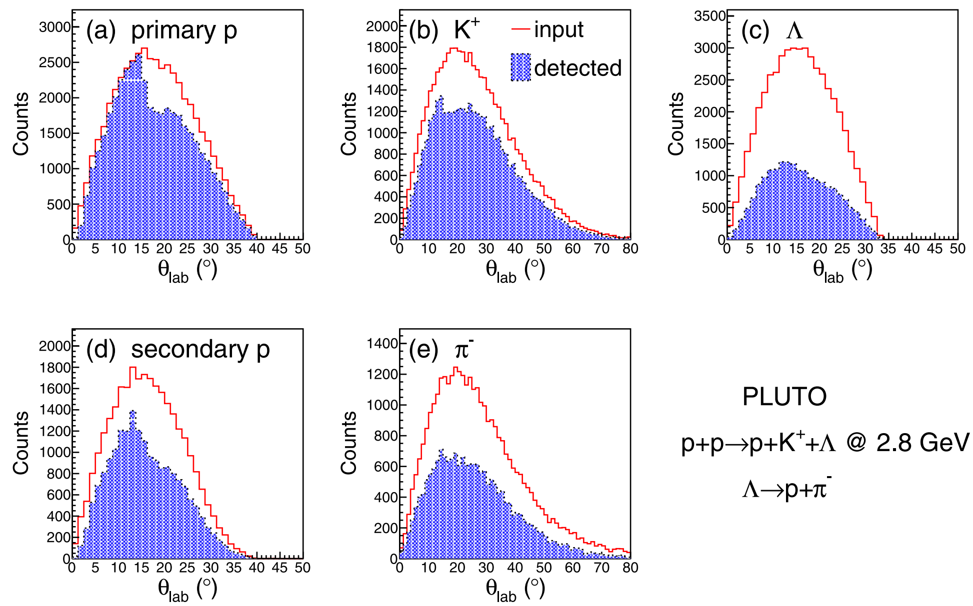

Fig. 8 (Color online) **a**–**c** Polar angle (θ_{lab}) distribution of final products of reaction pp→p$K^+\Lambda$ at 2.8 GeV simulated by the PLUTO generator; **d** and **e** shows θ_{lab} distribution of p and π^- decayed from Λ hyperon. The solid line and shielded region represent the distribution from simulation and those accepted by the CEE spectrometer

ideal spectrometer for studying frontier topics discussed in Sect. 1 at high-baryon density region, more detailed performance are described in Ref. [14].

4 Acceptance for pp→p$K^+\Lambda$ reaction

According to its design, HIRFL-CSR can provide a proton beam with a maximum energy of 2.8 GeV, allowing us to perform pp and pA reactions to investigate topics related to hadron physics [51], hypernuclei [25, 52] and so on. Studying the feasibility of conducting hadron physics studies through pp and pA reactions using the CEE spectrometer is crucial for expanding the physics scope of the CEE spectrometer and maximizing its scientific value.

The reaction pp→p$K^+\Lambda$ is a typical channel for verifying the detector performance. Λ hyperon is a short-lived particle with a lifetime of approximately 263 ps. It has a charged decay channel Λ→p + π^- with a decay branch ratio of approximately 64% [46]. If the four momenta of its two daughter particles can be measured, then Λ hyperon can be identified by reconstructing its invariant mass.

The phase space of pp→p$K^+\Lambda$ at 2.8 GeV was simulated with the PLUTO generator, and the polar angle (θ) distributions of the final products, that is p, K^+, Λ, as well as p and π^- decayed from Λ hyperon, are shown by the solid line in Fig. 8a–e, respectively. In this simulation, if the track length of a charged particle in the TPC is larger than 15 cm or it can pass through three MWDCs, it is considered a measurable particle. The fraction detectable by the CEE spectrometer is shown by the shaded distribution in each panel. Λ hyperon with two detectable daughter particles is treated as a detectable candidate, and approximately 37% of Λ hyperon is in the acceptance of the CEE spectrometer. The designed performance of the CEE spectrometer for charged particles is comparable to that of existing experiments, such as FOPI, HADES, and STAR. Therefore, the CEE spectrometer is expected to play a crucial role in experimentally investigating the aforementioned topics within pp, pA, and AA reactions at HIRFL-CSR energies.

5 Summary

In this study, an analysis and simulation software package (CeeROOT) for the CEE experiment is introduced. Based on the CEE conceptual design and CeeROOT package, optimization procedures, physical considerations, and optimization results for the CEE detector configuration are presented. The final optimized detector configuration serves as a blueprint for the final technical design of the CEE experiment. The acceptance of the CEE spectrometer for charged particles in U+U collisions at 500 MeV/u and pp→p$K^+\Lambda$ at 2.8 GeV are illustrated, demonstrating that the CEE experiment is an ideal spectrometer for studying frontier physics topics at HIRFL-CSR energies with pp, pA, and AA collisions. Currently, the components of the CEE experiment are under massive production, and the CEE spectrometer is expected to be commissioned in 2025.

Author Contributions All authors contributed to the study conception and design. Material preparation and data collection and analysis were performed by Jian-Wang Hong, Chen-Lu Hu, Xiong-Hong He, Zhi-Hui Xu, Zhi Qin, and Ya-Peng Zhang. The first draft of the manuscript was written by Ya-Peng Zhang, and all authors commented on previous versions of the manuscript. All authors read and approved the final manuscript.

Declarations

Conflict of interest De-Qing Fang is an editorial board member for Nuclear Science and Techniques and was not involved in the editorial review or the decision to publish this article. All authors declare that there are no conflict of interest.

References

1. L.P. Csernai, *Introduction to relativistic heavy ion collisions* (Wiley, New York, 1994)
2. W. Busza, K. Rajagopal, W. van der Schee, Heavy ion collisions: the big picture, and the big questions. Ann. Rev. Nucl. Part. Sci. **68**, 339–376 (2018). https://doi.org/10.1146/annurev-nucl-101917-020852
3. X. Luo, N. Xu, Search for the QCD critical point with fluctuations of conserved quantities in relativistic heavy-ion collisions at RHIC: an overview. Nucl. Sci. Tech. **28**, 112 (2017). https://doi.org/10.1007/s41365-017-0257-0
4. A. Bzdak, S. Esumi, V. Koch et al., Mapping the phases of quantum chromodynamics with beam energy scan. Phys. Rept. **853**, 1–87 (2020). https://doi.org/10.1016/j.physrep.2020.01.005
5. X. Luo, S. Shi, N. Xu et al., A study of the properties of the QCD phase diagram in high-energy nuclear collisions. Particles **3**, 278–307 (2020). https://doi.org/10.3390/particles3020022
6. J.H. Chen, X. Dong, X.H. He et al., Properties of the QCD matter: review of selected results from the relativistic heavy ion collider beam energy scan (RHIC BES) program. Nucl. Sci. Tech. **35**, 214 (2024). https://doi.org/10.1007/s41365-024-01591-2
7. J.M. Lattimer, Neutron stars and the nuclear matter equation of state. Ann. Rev. Nucl. Part. Sci. **71**, 433–464 (2021). https://doi.org/10.1146/annurev-nucl-102419-124827
8. Y.P. Zhang, Z.Y. Sun, G.C. Yong et al., Intermediate/high-energy heavy-ion collisions and nuclear matter equation of state. Acta Phys. Sin. **74**, 112101 (2025). https://doi.org/10.7498/aps.74.20241650
9. J. Steinheimer, A. Motornenko, A. Sorensen et al., The high-density equation of state in heavy-ion collisions: constraints from proton flow. Eur. Phys. J. C **82**, 911 (2022). https://doi.org/10.1140/epjc/s10052-022-10894-w
10. J.W. Xia, W.L. Zhan, B.W. Wei et al., The heavy ion cooler-storage-ring project (HIRFL-CSR) at Lanzhou. Nucl. Instrum. Meth. A **488**, 11–25 (2002). https://doi.org/10.1016/s0168-9002(02)00475-8
11. M. Zhang, Z.G. Xiao, B.A. Li et al., A Systematic study of the π^-/π^+ ratio in heavy-ion collisions with the same neutron/proton ratio but different masses. Phys. Rev. C **80**, 034616 (2009). https://doi.org/10.1103/PhysRevC.80.034616
12. F. Fu, Z.G. Xiao, Y.P. Zhang et al., Nuclear stopping and compression in heavy-ion collisions at intermediate energies. Phys. Lett. B **666**, 359–363 (2008). https://doi.org/10.1016/j.physletb.2008.07.063
13. L. Lü, H. Yi, Z. Xiao et al., Conceptual design of the HIRFL-CSR external-target experiment. Sci. China Phys. Mech. Astron. **60**, 012021 (2017). https://doi.org/10.1007/s11433-016-0342-x
14. D. Guo, X. He, P. Li et al., Studies of nuclear equation of state with the HIRFL-CSR external-target experiment. Eur. Phys. J. A **60**, 36 (2024). https://doi.org/10.1140/epja/s10050-024-01245-2
15. M.A. Stephanov, On the sign of kurtosis near the QCD critical point. Phys. Rev. Lett. **107**, 052301 (2011). https://doi.org/10.1103/PhysRevLett.107.052301
16. S. Wu, The sign of kurtosis within finite system near the QCD critical point. Nucl. Sci. Tech. **36**, 149 (2025). https://doi.org/10.1007/s41365-025-01721-4
17. M.S. Abdallah and B.E. Aboona and J. Adam et al., Disappearance of partonic collectivity in $\sqrt{s_{NN}}$=3 GeV Au+Au collisions at RHIC. Phys. Lett. B **827**, 137003 (2022). https://doi.org/10.1016/j.physletb.2022.137003
18. J. Adamczewski-Musch, O. Arnold, C. Behnke et al., Proton-number fluctuations in $\sqrt{s_{NN}}$ =2.4 GeV Au + Au collisions studied with the High-Acceptance DiElectron Spectrometer (HADES). Phys. Rev. C **102**, 024914 (2020). https://doi.org/10.1103/PhysRevC.102.024914
19. S. Huth, P.T.H. Pang, I. Tews et al., Constraining neutron-star matter with microscopic and macroscopic collisions. Nature **606**, 276–280 (2022). https://doi.org/10.1038/s41586-022-04750-w
20. B.A. Li, B.J. Cai, L.W. Chen et al., A theoretical overview of isospin and EOS effects in heavy-ion reactions at intermediate energies. Nuovo Cim. C **45**, 54 (2022). https://doi.org/10.1393/ncc/i2022-22054-3
21. L.W. Chen, Higher order bulk characteristic parameters of asymmetric nuclear matter. Sci. China Phys. Mech. Astron. **54**, 124–129 (2011). https://doi.org/10.1007/s11433-011-4415-9
22. T. Song, L. Tolos, J. Wirth et al., In-medium effects in strangeness production in heavy-ion collisions at (sub)threshold energies. Phys. Rev. C **103**, 044901 (2021). https://doi.org/10.1103/PhysRevC.103.044901
23. R. Wang, Y.G. Ma, L.W. Chen et al., Kinetic approach of light-nuclei production in intermediate-energy heavy-ion collisions. Phys. Rev. C **108**, L031601 (2023). https://doi.org/10.1103/PhysRevC.108.L031601
24. B.A. Li, W.J. Guo, Z. Shi, Effects of the kinetic symmetry energy reduced by short-range correlations in heavy-ion collisions at intermediate energies. Phys. Rev. C **91**, 044601 (2015). https://doi.org/10.1103/PhysRevC.91.044601
25. S. Zhang, J.H. Chen, Y.G. Ma et al., Hypernucleus production at RHIC and HIRFL-CSR energy. Int. J. Mod. Phys. E **19**, 1829 (2010). https://doi.org/10.1142/S0218301310016260
26. W. Huang, F. Lu, H. Li et al., Laser test of the prototype of CEE time projection chamber. Nucl. Sci. Tech. **29**, 41 (2018). https://doi.org/10.1007/s41365-018-0382-4
27. X. Wang, D. Hu, M. Shao et al., CEE inner TOF prototype design and preliminary test results. J. Instrum. **17**, P09023 (2022). https://doi.org/10.1088/1748-0221/17/09/P09023
28. L.M. Lyu, H. Yi, L.M. Duan et al., Simulation and prototype testing of multi-wire drift chamber arrays for the CEE. Nucl. Sci. Tech. **31**, 11 (2020). https://doi.org/10.1007/s41365-019-0716-x
29. Z.B. He, Z. Qin, P. Ma et al., Development of a MWDC prototype of the CSR external-target experiment. Nucl. Sci. Tech. **35**, 174 (2024). https://doi.org/10.1007/s41365-024-01515-0
30. Z. Qin, Z. He, Z. Cao et al., Beam test results of the prototype of the multi wire drift chamber for the CSR external-target experiment. Nucl. Sci. Tech. **36**, 67 (2025). https://doi.org/10.1007/s41365-024-01628-6
31. B. Wang, D. Han, Y. Wang et al., The CEE-eTOF wall constructed with new sealed MRPC. J. Instrum. **15**, C08022 (2020). https://doi.org/10.1088/1748-0221/15/08/C08022
32. S.H. Zhu, H.B. Yang, H. Pei et al., Prototype design of readout electronics for Zero Degree Calorimeter in the HIRFL-CSR external-target experiment. J. Instrum. **16**, P08014 (2021). https://doi.org/10.1088/1748-0221/16/08/P08014
33. J. Liu, C.S. Gao, H.L. Wang et al., Readout electronics for beam monitor in the external-target experiment of CSR. Nucl. Sci. Tech. **36**, 87 (2025). https://doi.org/10.1007/s41365-025-01652-0
34. L.K. Liu, H. Pei, Y.P. Wang et al., Event plane determination from the zero degree calorimeter at the cooling storage ring external-target experiment. Nucl. Sci. Tech. **34**, 100 (2023). https://doi.org/10.1007/s41365-023-01262-8

35. M. Al-Turany, D. Bertini, R. Karabowicz et al., The FairRoot framework. J. Phys. Conf. Ser. **396**, 022001 (2012). https://doi.org/10.1088/1742-6596/396/2/022001
36. R. Brun, F. Bruyant, M. Maire et al., GEANT3 user's guide. CERN DD/EE/84-1. Computing and Networks Division, CERN, 1994
37. S. Agostinelli, J. Allison, K. Amako et al., GEANT4-a simulation toolkit. Nucl. Instrum. Meth. A **506**, 250–303 (2003). https://doi.org/10.1016/S0168-9002(03)01368-8
38. M. Bleicher, E. Zabrodin, C. Spieles et al., Relativistic hadron hadron collisions in the ultrarelativistic quantum molecular dynamics model. J. Phys. G **25**, 1859–1896 (1999). https://doi.org/10.1088/0954-3899/25/9/308
39. O. Buss, T. Gaitanos, K. Gallmeister et al., Transport-theoretical description of nuclear reactions. Phys. Rept. **512**, 1–124 (2012). https://doi.org/10.1016/j.physrep.2011.12.001
40. W. Cassing, E.L. Bratkovskaya, Parton-Hadron-String Dynamics: an off-shell transport approach for relativistic energies. Nucl. Phys. A **831**, 215–242 (2009). https://doi.org/10.1016/j.nuclphysa.2009.09.007
41. N. Ikeno, A. Ono, Y. Nara et al., Probing neutron-proton dynamics by pions. Phys. Rev. C **93**, 044612 (2016) [erratum: Phys. Rev. C **97**, 069902 (2018)] https://doi.org/10.1103/PhysRevC.93.044612
42. C. Hartnack, R.K. Puri, J. Aichelin et al., Modeling the many body dynamics of heavy ion collisions: Present status and future perspective. Eur. Phys. J. A **1**, 151–169 (1998). https://doi.org/10.1007/s100500050045
43. Y. Nara, A. Ohnishi, Mean-field update in the JAM microscopic transport model: Mean-field effects on collective flow in high-energy heavy-ion collisions at $\sqrt{s_{\rm NN}}$=2–20 GeV energies. Phys. Rev. C **105**, 014911 (2022). https://doi.org/10.1103/PhysRevC.105.014911
44. Z.Q. Feng, Momentum dependence of the symmetry potential and its influence on nuclear reactions. Phys. Rev. C **84**, 024610 (2011). https://doi.org/10.1103/PhysRevC.84.024610
45. I. Fröhlich, L. Cazon Boado, T. Galatyuk et al., Pluto: a Monte Carlo simulation tool for hadronic physics. PoS **ACAT**, 076 (2007). https://doi.org/10.22323/1.050.0076
46. S. Navas, C. Amsler, T. Gutsche et al., Review of particle physics. Phys. Rev. D **110**, 030001 (2024). https://doi.org/10.1103/PhysRevD.110.030001
47. E. Lamour, P.D. Fainstein, M. Galassi et al., Extension of charge-state-distribution calculations for ion-solid collisions towards low velocities and many-electron ions. Phys. Rev. A **92**, 042703 (2015). https://doi.org/10.1103/PhysRevA.92.042703
48. B. Zhang, L.K. Liu, H. Pei et al., Classifier for centrality determination with zero-degree calorimeter at the cooling-storage-ring external-target experiment. Nucl. Sci. Tech. **34**, 176 (2023). https://doi.org/10.1007/s41365-023-01338-5
49. A. Gobbi, J.P. Alard, G. Augustinski et al., A highly segmented ΔE time-of-flight wall as forward detector of the 4π system for charged particles at the SIS / ESR accelerator. Nucl. Instrum. Meth. A **324**, 156–176 (1993). https://doi.org/10.1016/0168-9002(93)90974-M
50. J. Adams, A. Ewigleben, S. Garrett et al., The STAR event plane detector. Nucl. Instrum. Meth. A **968**, 163970 (2020). https://doi.org/10.1016/j.nima.2020.163970
51. C. Zheng, Z.G. Xiao, H.S. Xu et al., Hadron physics programs at HIRFL-CSRm: plan and status. Chin. Phys. C **31**, 1177–1180 (2007)
52. J.T. Balewski, A. Budzanowski, H. Dombrowski et al., Total cross-section of the reaction $pp \rightarrow pK^+\Lambda$ close to threshold. Phys. Lett. B **420**, 211–216 (1998). https://doi.org/10.1016/S0370-2693(97)01527-X

Authors and Affiliations

Jian-Wang Hong[1,2] · Chen-Lu Hu[1,2] · Yu-Hong Yu[1,2,3] · Nu Xu[1,2,3] · Zhi-Yu Sun[1,2,3] · Hao Qiu[1,2,3] · Zhi-Gang Xiao[4] · Ming Shao[5] · Li-Min Duan[1,2,3] · Xiong-Hong He[1,2,3] · Zhi-Hui Xu[1] · Yi Wang[6] · Dong Han[6] · Zi-Xuan Chen[1,2] · Feng-Yi Zhao[1,2,3] · He-Run Yang[1,2] · Xiang-Lun Wei[1,2] · Rong-Jiang Hu[1,2] · Feng Liu[7] · Hua Pei[7] · Ya-Ping Wang[7] · Ye Tian[1,2] · Zhi Qin[4] · Dong-Dong Hu[5] · Guo-Dong Shen[1,2] · Li-Jun Mao[1,2] · Wei Wu[1,2] · Wei You[1,2] · Yu-Quan Chen[1,2] · Peng Yang[1,2] · De-Qing Fang[8,9] · Ya-Peng Zhang[1,2,3]

✉ Xiong-Hong He
hexh@impcas.ac.cn

✉ Zhi-Hui Xu
xuzh@impcas.ac.cn

✉ Zhi Qin
qinz18@mails.tsinghua.edu.cn

✉ Ya-Peng Zhang
y.p.zhang@impcas.ac.cn

1 Institute of Modern Physics, Chinese Academy of Sciences, Lanzhou 730000, China

2 School of Nuclear Science and Technology, University of Chinese Academy of Sciences, Beijing 100084, China

3 State Key Laboratory of Heavy Ion Science and Technology, Institute of Modern Physics, Chinese Academy of Sciences, Lanzhou 730000, China

4 Department of Physics, Tsinghua University, Beijing 100084, China

5 Department of Modern Physics, University of Science and Technology of China, Hefei 230026, China

6 Department of Engineering Physics, Tsinghua University, Beijing 100084, China

7 Key Laboratory of Quark and Lepton Physics and Institute of Particle Physics, Central China Normal University, Wuhan 430079, China

8 Key Laboratory of Nuclear Physics and Ion-beam Application (MOE), Fudan University, Shanghai 200433, China

9 Shanghai Research Center for Theoretical Nuclear Physics, NSFC and Fudan University, Shanghai 200438, China